Carbon formation mechanism of C_2H_2 in Ni-based catalysts revealed by in situ electron microscopy and molecular dynamics simulations

Sun, Chunwen; Su, Rui; Chen, Jian; Lu, Liang; Guan, Pengfei

Publisher's version / Version de l'éditeur:
https://doi.org/10.1021/acsomega.9b00958
ACS Omega, 4, 5, pp. 8413-8420, 2019-05-13

ACS OMEGA

Article

Cite This: ACS Omega 2019, 4, 8413−8420

http://pubs.acs.org/journal/acsodf

Carbon Formation Mechanism of C_2H_2 in Ni-Based Catalysts Revealed by in Situ Electron Microscopy and Molecular Dynamics Simulations

Chunwen Sun,*[,†,‡,#] Rui Su,[§,⊥] Jian Chen,*[,∥] Liang Lu,[†] and Pengfei Guan*[,§]

[†]CAS Center for Excellence in Nanoscience, Beijing Institute of Nanoenergy and Nanosystems, Chinese Academy of Sciences, Beijing 100083, P. R. China

[‡]School of Nanoscience and Technology, University of Chinese Academy of Sciences, Beijing 100049, P. R. China

[§]Beijing Computational Science Research Center, Beijing 100193, P. R. China

[∥]Nanotechnology Research Centre, National Research Council Canada (NRC), Edmonton, Alberta T6G 2M9, Canada

[⊥]Innovative Center for Advanced Materials, Hangzhou Dianzi University, Hangzhou 310018, P. R. China

[#]Center on Nanoenergy Research, School of Physical Science and Technology, Guangxi University, Nanning 530004, P. R. China

Supporting Information

ABSTRACT: Understanding the carbon formation mechanism is critical for designing catalysts in various applications. Here, we report the observation of the carbon formation mechanism on Ni-based catalysts by environmental transmission electron microscopy (ETEM) over a wide temperature range in combination with molecular dynamics simulations and density functional theory calculations. In situ TEM observation performed in a C_2H_2/H_2 atmosphere provides real-time evidence that Ni_3C is an intermediate phase that decomposes to graphitic carbon and metallic Ni, leading to carbon formation. Mechanisms of acetylene decomposition and evolution of carbon atom configuration are revealed by molecular dynamics simulations, which corroborate the experimental results. The modification of MgO on NiO can effectively decrease the formation of graphitic layers and thus enhance the catalytic performance of NiO. This finding may provide an insight into the origin of the carbon deposition and aid in developing effective approaches to mitigate it.

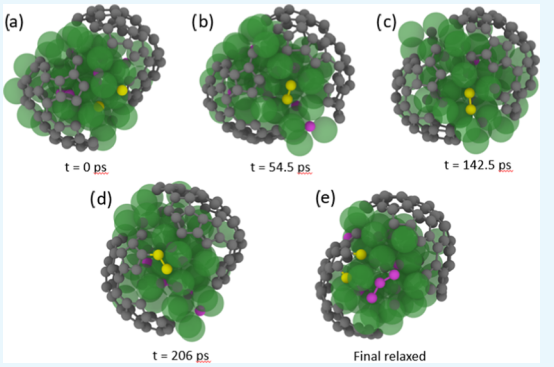

INTRODUCTION

Understanding the carbon formation mechanism is critical for many technical applications, including steam reforming, methanation, and solid oxide fuel cells (SOFCs).[1−7] SOFCs are the most efficient and benign energy conversion devices for wide applications from portable and transportation power to stationary plants.[8] The operation of SOFCs with various hydrocarbon-based fuels has attracted much attention during the last decade. Although nickel has excellent catalytic activity and is a good steam-reforming catalyst, the Ni-cermet anodes tend to suffer from carbon deposition (coking) and sulfur poisoning in hydrocarbon fuels.[9,10] Thus, the development of nickel-free conducting metal oxides has been a subject of considerable interest. Perovskites, $La_{0.75}Sr_{0.25}Cr_{0.5}Mn_{0.5}O_{3-\delta}$,[11] $(La,Sr)TiO_3$,[12] $BaZr_{0.1}Ce_{0.7}Y_{0.2-x}Yb_xO_{3-\delta}$,[13] and double-perovskites, $Sr_2Mg_{1-x}Mn_xMoO_{6-\delta}$,[9] have been reported as possible alternative anode materials. They showed improved tolerance to coking, reoxidation, and/or sulfur poisoning under various SOFC operating conditions. However, the power densities of the SOFCs with these anodes are still not satisfactory compared with conventional Ni cermet anodes.[13] Therefore, all of these anode materials have not yet been used in practical SOFC systems. Recently, we demonstrated enhanced tolerance to coking of the Ni cermet anode in hydrocarbon-fueled SOFCs by impregnating a small amount of MgO (1.25−3.75 wt %) into the porous anode.[14] Owing to the complexity of the heterogeneous reaction mechanism for CH_4 oxidation,[15] the carbon formation mechanism remains to be elucidated. Density functional theory (DFT) calculations or in situ and ex situ experimental techniques combined with DFT calculations have been developed to address this problem,[16−21] but revealing the mechanism of catalytic carbon growth is still a challenging task. Here, we study a MgO-modified NiO catalyst under a C_2H_2/H_2 atmosphere in the temperature range in which SOFCs operate, using in situ transmission electron microscopy (TEM), in an attempt to unravel the carbon formation mechanism. It is found that Ni_3C is an intermediate phase during the carbon deposition process. The modification

Received: April 4, 2019
Accepted: May 3, 2019
Published: May 13, 2019

of MgO on NiO can effectively decrease the formation of graphitic layers and thus enhance the catalytic performance of NiO. Acetylene decomposition, carbon solute reduction, and surface carbon shell evolution are provided by molecular dynamics simulations. The origin of the enhanced coking-resistant performance of the MgO-modified NiO catalyst is ascribed to the improved thermodynamic stability of lattice oxygens.

EXPERIMENTAL METHODS

Material Preparation. NiO powders were synthesized by a glycine-nitrated combustion process.[22] The MgO-modified NiO was prepared by impregnating a solution of magnesium acetate [$MgO(CH_3COO)_2{\cdot}4H_2O$] into the NiO powders and annealing at 400 °C for 1 h. The MgO loading is about 2 wt %.

Material Characterization. The crystal structures of the as-prepared NiO and MgO-modified NiO were examined by X-ray diffraction (XRD) measurements (Panalytical instrument X'Pert 3 Powder) with Cu Kα radiation in the 2θ range of 20−80°. The morphology and microstructure of the sample were observed on a transmission electron microscope at a working voltage of 200 kV (JEOL JEM-2200FS).

In Situ TEM Characterization. A small quantity of the above prepared powder was dispersed in deionized water in an ultrasonic bath for 20 min. Several drops of the solution were put on a Si window with a continuous silicon nitride thin film (Dura SiN), in which there are homogeneously distributed 2 μm holes with 10 μm spacing between the holes. After the solution was dried in air, the Dura SiN was mounted on a Gatan single tilt heating holder.

A Hitachi H-9500 environmental transmission electron microscope (ETEM) was employed in the current investigation. The electron source of the current H-9500 ETEM is LaB_6. To further decrease the beam damage to the specimen, the beam was kept off during the heating process unless an image or diffraction pattern was being collected. A slow heating rate is beneficial for NiO to get fully reduced and for the TEM specimen to decrease thermal drift. However, the pumping out of the H_2 + C_2H_2 gases released into the TEM specimen chamber relies on a single high-speed turbo molecular pump (TMP). A long pumping time will fail the TMP by overheating. Therefore, a reasonably slow heating rate and a low-pressure level (e.g., 10 °C/min and 0.15 Pa, respectively) were chosen in this experiment to avoid the overload of the TMP.

Simulations. The C_2H_2 decomposition and carbon deposition are simulated by the molecular dynamics package LAMMPS. The reactive force field, ReaxFF, is used to describe the interactions of the atoms and the formation/breaking of the chemical bonds.[23] The ReaxFF parameters are taken from the literature,[24] which are specially fitted to describe the Ni and hydrocarbon systems. The time step is specified to 0.25 fs. At each deposition stage, a single carbon atom is randomly deposited near the surface of the Ni cluster. Minimization is then performed to remove the spurious forces in the system. Microcanonical equilibration is then performed at 300 K, where the total atom number (N), the temperature (T), and the volume (V) for the system are fixed, and a Bussi thermostat is then employed. The system is first brought to the target temperature of 1600 K, and then kept at 1600 K for 225 ps. Finally, the prolonged relaxation effect is accounted for by performing another 100 000 steps of force-biased Monte-Carlo simulation with a displacement of 0.1 Å.[25] This stage is repeated until the carbon atoms needed are deposited.

First-principles calculations are performed by the Vienna ab initio package. The wave functions are expanded using a plane-wave cutoff of 400 eV. The valence core interactions are described by the projected augmented-wave method. A 3 × 3 × 3 Monkhorst−Pack K-mesh is used to sample the Brillouin zone. All structures are relaxed until the force amplitudes are less than 0.05 eV/Å. Exchange−correlation effects are described by the Perdew−Burke−Ernzerhof functional within the generalized gradient approximation. The strong correlation effect of Ni 3d orbital is addressed by the DFT + U method with an effective U = 4.2 eV. Due to the poor description of DFT of the O_2 ground state, the O_2 energy is corrected against H_2O and H_2 energies to reproduce the measured H_2O formation energy.

RESULTS AND DISCUSSION

In Situ TEM Characterization. In an attempt to accelerate the carbon deposition, a mixture of C_2H_2/H_2 (volume ratio = 1:4), rather than CH_4 or C_3H_8 commonly used as fuels in hydrocarbon-fueled SOFCs, was employed. Figure S1 (Supporting Information) shows XRD patterns of NiO and MgO-modified NiO samples. Figure S2 shows an annular dark-field (ADF) scanning transmission electron microscopy (STEM) image and the line-scanning profiles of elements across one particle. It can be seen that NiO particles are covered with MgO nanoparticles. Figure 1b−e shows snapshots of NiO and MgO-modified NiO catalysts at ambient temperature and 800 °C in C_2H_2/H_2, respectively. For the NiO catalyst, it can be seen that Ni particles are encapsulated by thick graphitic layers at 800 °C, as indicated by the arrows for a comparison. However, for the MgO-modified NiO catalyst, there are no obvious graphitic layers wrapping Ni particles (indicated by red arrows). The corresponding videos of NiO and MgO-modified NiO are shown as Supporting Materials Videos 1 and 2, respectively. Furthermore, Figure S4 shows a graphitic layer comparison between the NiO and the MgO-modified samples. In an alternative region of the same in situ experiment for the NiO sample, thick graphitic layers can be seen (Figure S3a), which can be easily identified from their typical layer feature. The electron energy loss spectrum collected confirms this observation. Figure S3b displays the same region as Figure 1e. From the high-resolution TEM (HRTEM) image, we can see that the graphitic layers are formed, but their thickness is greatly reduced compared with those in Figure S3a.

Figure 2 shows the in situ evolution of the selected area electron diffraction (SAED) pattern with temperature for NiO and MgO-modified NiO, respectively. In the collected ring patterns, the same ring and its indexed phase(s) are marked by arrows and text with the same color. The overlapping of the main diffractions of NiO, Ni, and hexagonal Ni_3C brings difficulty to the ring pattern indexation. Among them, although NiO(111) overlaps Ni_3C(104), it still can be considered as an indication of the existence of NiO due to the very high intensity of NiO(111) compared with Ni_3C(104). There is no overlapping of Ni(200) with NiO and Ni_3C, and thus Ni(200) can be used as an indication of the appearance of Ni. The Ni(200) diffraction is seen (the first green arrow in Figure 2A) for the NiO sample heated at 432 °C. In their study of reduction of nickel oxide by hydrogen, Jeangros et al. found the diffraction of Ni(200) appeared at 405 °C.[26] Because we

DOI: 10.1021/acsomega.9b00958
ACS Omega 2019, 4, 8413−8420

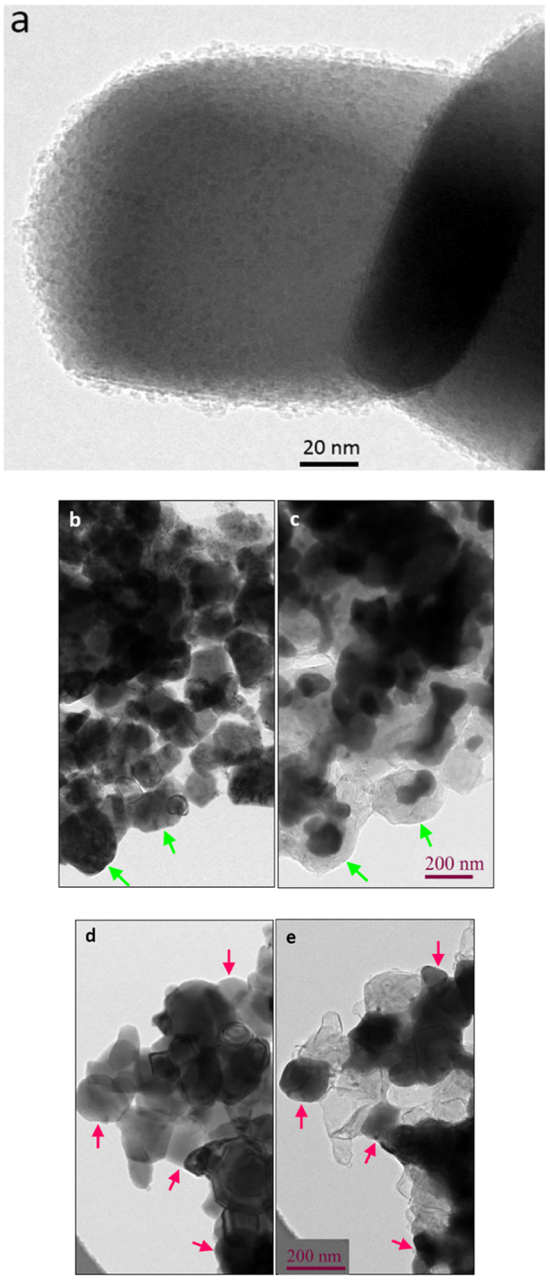

Figure 1. TEM images of (a) as-prepared MgO-modified NiO sample, (b) NiO catalyst in C_2H_2/H_2 at room temperature, (c) NiO catalyst in C_2H_2/H_2 at 800 °C, (d) MgO-modified NiO catalyst in C_2H_2/H_2 at room temperature, and (e) MgO-modified NiO catalyst in C_2H_2/H_2 at 800 °C.

applied a large time gap between the sequential image/diffraction collection to lessen beam damage to the sample, we could not monitor the time at which the appearance of Ni(200) diffraction started, even though our result agrees with Jeangros's result fairly well if we only consider the reduction of H_2. At 625 °C, we did not find NiO(111) diffraction, which suggests that NiO reduction has been completed prior to 625 °C. Because C_2H_2 coexists with H_2 in this investigation, rather than a reduction reaction between H_2 and NiO, C_2H_2 can also be involved through the reactions below.[27]

$$6NiO + C_2H_2 + H_2 = 6Ni + 2CO_2 + 2H_2O \quad (1)$$

and/or

$$3NiO + C_2H_2 + H_2 = Ni_3C + CO + 2H_2O \quad (2)$$

The thermodynamic calculation shows that the free standard reaction enthalpies of eqs 1 and 2 are −140 and −120 kJ/mol, respectively.[28,29] Thus it indicates that both eqs 1 and 2 are thermodynamically possible in the current investigation temperature range. When C_2H_2 adsorbed at Ni (111)/O (2×2) was heated up to 325 °C, the observation of CO formation suggests that reaction (2) is more favorable.[30]

The reshaping of the metal catalysts is a common phenomenon during the formation of carbon nanotube (CNT).[16,31−34] Hofmann et al. found the "liquid-like" feature of Ni during the growth of CNT.[31] They attributed it to the fast self-diffusivity of Ni. The melting temperature for pure Ni is 1455 °C.[35] Under equilibrium condition, when the addition of carbon reaches around 2.8 atom %, the melting temperature of Ni(C) decreases to 1326.5 °C.[36] Rapid cooling can bring the solubility of carbon in Ni up to 7.9 atom % (hereafter, we denote C-added Ni as Ni(C)) and bring the melting temperature of Ni(C) down to around 1025 °C.[36] Carbon-rich phase diagrams of Ni−C nanoparticles show that Ni(C) nanoparticle melting is strongly favored by carbon incorporation and proceeds from the surface to the core.[37] Supporting Materials Video 3 shows that the melting of Ni(C) and graphitic layer formation proceed simultaneously. Based on the above discussion, we postulate that both reactions 1 and 2 happen and that Ni_3C formed by reaction 2 decomposes to Ni(C) and carbon, and then the carbon goes into the metal Ni matrix reduced by reaction 1 to rapidly increase its carbon content. This, in turn, lowers the melting temperature of Ni(C) and turns Ni(C) into the molten state at a relatively low heating temperature. Therefore, the diffraction, which is initially assigned to both NiO(220) and Ni_3C(116), now can be solely assigned to Ni_3C(116) (red arrow in Figure 2A). Similarly, diffraction that was assigned to NiO(200) before is assigned to Ni(111) and Ni_3C(116) (cyan arrows). When NiO was heated up to 800 °C, Ni_3C(116) diffraction vanished. Meanwhile, the diffraction of C(002) becomes stronger. Obviously, Ni_3C fully decomposes to Ni(C) and C.

The SAED pattern of MgO-modified NiO does not exhibit a well-defined ring pattern until the heating temperature reaches 565 °C. The ring pattern at 565 °C is quite similar to that of NiO at 550 °C, except for the diffraction belonging to carbon (e.g., C(002)) being present in the latter (white arrow in Figure 2A), whereas there is no detectable graphitic carbon in MgO-modified NiO. When the heating temperature reaches 625 °C, there is still no obvious C(002) ring in the SAED pattern of MgO-modified NiO, but C(002) diffraction is very apparent in that of the NiO sample. Unlike NiO, NiO(111) diffraction in MgO-modified NiO is still visible at 625 °C. It seems that the addition of MgO to NiO postpones the full reduction of NiO. In addition, even after longer time at 800 °C, the diffraction of Ni_3C(116) still exists for MgO-modified NiO and the C(002) diffraction is less intensive compared with that of NiO. Therefore, we postulate that the addition of MgO to NiO postpones the full decomposition of Ni_3C, which in turn leads to less graphitic carbon formation in MgO-modified NiO.

To unveil the mechanism of carbon deposition in NiO and MgO-modified NiO, another set of in situ experiments were conducted. In this set of runs, a higher magnification was employed. Figure 3 shows snapshots of high-resolution TEM (HRTEM) videos of graphitic layer formation in NiO and

DOI: 10.1021/acsomega.9b00958
ACS Omega 2019, 4, 8413−8420

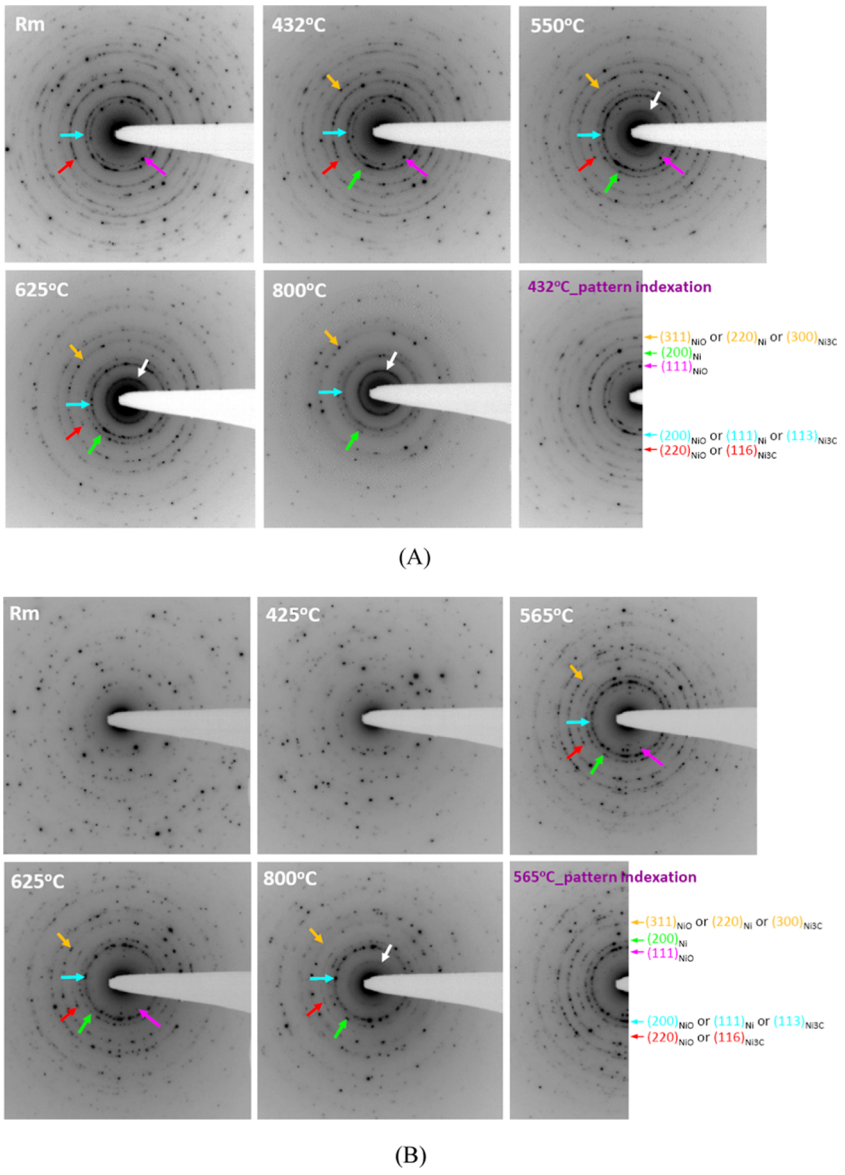

Figure 2. Evolution of the SAED pattern with temperature: (A) NiO; (B) MgO-modified NiO. See text for the discussion of the ring pattern diffraction assignments.

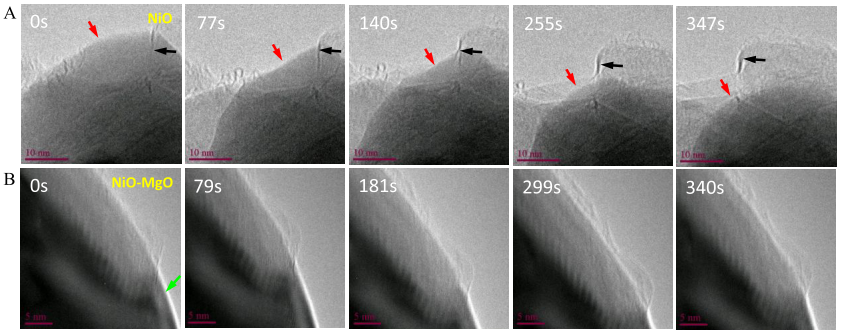

Figure 3. (A) Snapshot of the advancing edge of the graphitic layer in NiO and (B) Formation of the graphitic layer from a modulation region in MgO-modified NiO.

MgO-modified NiO, respectively. The black arrow in Figure 3A illustrates the advancing direction of the graphitic layers. Although the carbon deposition layer keeps advancing, the size of the Ni(C) particle shrinks in the direction indicated by the red arrow until the Ni(C) particle is encapsulated by the graphitic layer. Compared with NiO, the graphitic layer thickness in MgO-modified NiO is thinner and does not change much with time. Besides, the shape of the particle remains the same. The green arrow in the image indicates the surface without an obvious graphitic layer.

DOI: 10.1021/acsomega.9b00958
ACS Omega 2019, 4, 8413−8420

On close observation of the region where the carbon layers generate, as indicated by the black arrows in Figure 4, we find

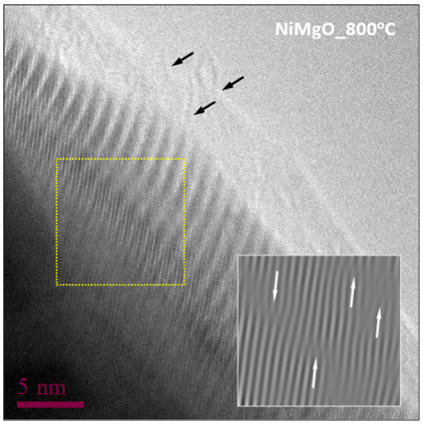

Figure 4. Modulation region in MgO-modified NiO. The black arrows indicate the carbon layers generating from the modulation region. The inset shows the existence of the dislocation within the structure.

that the carbon layers come from a modulated region. Since modulation is usually related to an intermediate phase between phase changes,[38] we believe that the formation of the graphitic layers results from the decomposition of modulated carbide. Besides, there is no melting phenomenon happening during this process. This possibly explains the slower graphitic layer growth rate as compared with that in NiO. Fourier transformation image processing on the chosen area within the modulated carbide region (marked by a square) shows the existence of the dislocation within the structure (marked by arrows in the inset in Figure 4). This is due to the strain induced by the decomposition of carbide. The results revealed by Figure 4 suggest that there are possible different mechanisms governing graphitic layer formation in NiO and MgO-modified NiO, respectively. Heracleous et al. found that it is extremely difficult to reduce Ni−Mg−O mixed metal oxides.[39] They attribute it to the solid solution formed between NiO and MgO.[39] The actual mechanism will be discussed in the following section.

Mechanistic Insights on Carbon Deposition. In the Experimental Methods section, we have shown that adding MgO to the NiO host is effective for reducing the deposition of carbon atoms. However, the detailed mechanism is not very well-established due to the limitation of the in situ observation itself. Therefore, we employ combined reactive molecular dynamics and density functional theory (DFT) simulations to reveal the microscopic mechanism of carbon deposition on MgO-modified NiO. Due to the complexity of the problem, we first focus on the following two issues: (1) the dynamical process of carbon shell formation on the Ni metal cluster; (2) the origin of enhanced structure stability of the NiO host by MgO addition.

To address the first issue, we modeled the carbon atom deposition process by a two-step process consisting of acetylene decomposition and carbon atom reduction. In the first step, an acetylene molecule is pinned near a melted-quenched Ni_{55} cluster. The whole system is then gradually heated to 1600 K and equilibrated for 250 ps. The whole decomposition process is shown in Figure 5. The acetylene molecule is first adsorbed at the Ni cluster surface at t = 0 ps.

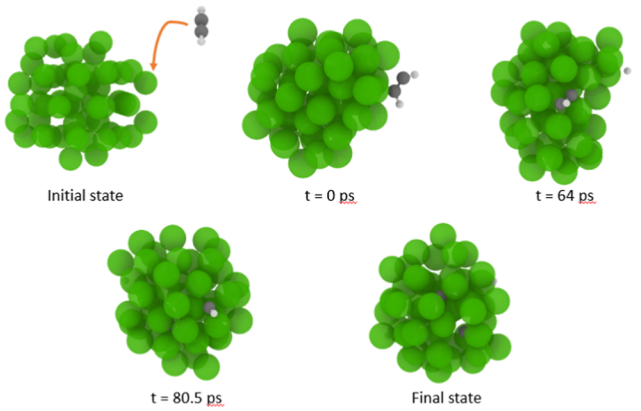

Figure 5. Molecular dynamics simulations of acetylene decomposition on the Ni_{55} cluster. The Ni, C, and H atoms are shown as large green, medium gray, and small white balls, respectively.

Then, the acetylene is decomposed to the pair of separated H−C≡C group and adsorbed hydrogen atom at t = 64 ps. Then, the H−C≡C group is further decomposed into a CH group and a solute C atom. Finally, the acetylene is decomposed into two solute C atoms and two adsorbed H atoms. The acetylene decomposition is several orders faster than the carbon shell formation process, which allows us to model the carbon deposition and reduction processes without explicitly considering the hydrogen atoms.

For the second step, the reduction process of solute carbon atoms is modeled. At first, we model the growth process of the surface carbon shell by periodically adding carbon atoms to the surface of the Ni cluster and relaxing the cluster by employing a hybrid MD/MC algorithm. The relationship between the number of solute C atoms and the number of total C atoms (N) is shown in Figure 6a. Ten indepedent simulations are performed to calculate the error bar. The whole process can be divided into three stages. First, all adsorbed carbon atoms migrate into the Ni cluster for $N \leq 20$ and a Ni−C solution is formed. When N is more than 20, the number of solute C

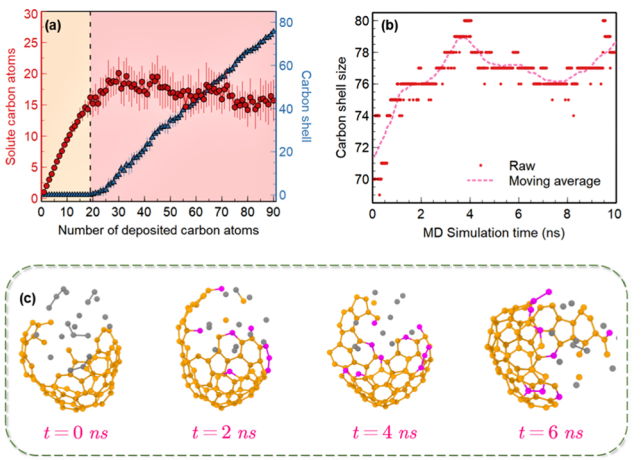

Figure 6. Evolution of surface and solute carbon atoms. (a) Evolution of the number of solute carbon atoms (red circles) and the carbon shell size (blue triangles) with respect to deposited carbon atoms. (b, c) Long-term evolution of the carbon shell size and local structure on the Ni cluster. The initial and later incorporated C atoms in the shell are shown as orange and pink balls and the rest of the C atoms are shown as gray balls. All Ni atoms are hidden for visualization.

DOI: 10.1021/acsomega.9b00958
ACS Omega 2019, 4, 8413−8420

atoms remains around 20 and is slightly reduced as N increases. At the same time, formation and growth of the surface carbon shell proceeds at this stage. It is worth to note that at the end of the first stage, the molar ratio of Ni/C is in the range of 3.2−4.2, which is close to the chemical formula of Ni_3C. Considering the extra surface Ni atoms, the observed maximum of the carbon solute number is most likely due to the saturation of solute carbon atoms. It might be of special interest to determine whether a crystal-like Ni_3C can be found in the core of the Ni cluster. However, since the Ni cluster is small and exhibits strong interaction with the carbon shell, the local strain is too large to preserve the crystal structure. Furthermore, as shown in Figure 6a, the reduction of the carbon solute is very gentle due to the limited simulation time at each MD/MC stage. To simulate the long-term effect on the evolution of the surface carbon shell, one sample of $N = 90$ is chosen for another long 10 ns simulation at higher temperatures to accelerate the reduction process. The size and structure evolutions are shown in Figure 6b,c. After 4 ns, the surface carbon shell reaches a maximum size of 80 in comparison with the initial size of 70. Then, the shell size oscillates around 78. Since the growth of the carbon shell is inherently a rare event, we expect that the Ni/C solute will be fully reduced to Ni and the carbon shell at lower temperatures and a much longer time scale, as observed in the aforementioned experiment.

For the detailed process of carbon shell growth, we tracked the position of two carbon atoms in an intermediate trajectory for $N = 96$, as shown in Figure 7. The tracked, network, and

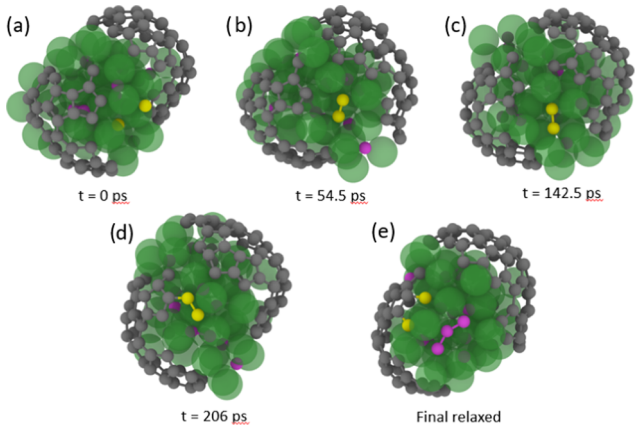

Figure 7. Growth dynamics of the surface carbon network: (a) 0 ps, (b) 54.5 ps, (c) 142.5 ps, (d) 206 ps, and (e) final relaxed. The Ni atoms are shown as green semitransparent balls. The carbon atoms are shown as small balls with different colors. The yellow-colored ones denote the tracked atoms. The carbon network is colored dark gray. The other carbon atoms are colored pink.

other carbon atoms are shown by yellow, gray, and pink colors, respectively. Initially, the two carbon atoms are well-separated by Ni atoms and stay on the subsurface and the surface of the Ni cluster (Figure 7a), respectively. The two atoms then form a C−C dimer on the cluster surface (Figure 7b,c). As the C−C dimer diffuses on the cluster surface, it reaches and bonds to a nearby edge site of the carbon network and extends the original network. To shed light on the kinetic process of the solute carbon atoms, additional simulation is performed from the last Ni−C structure without adding new surface carbon atoms. In Supporting Materials Video 4, we show how a solute carbon atom is gradually decomposing from the Ni core and extending the carbon shell. Our simulation result shows that the growth of the surface carbon network can grab carbon atoms, which dissolute to the cluster surface. As the growth of the carbon network happens at the edge sites, the reduction of the solute carbon atoms can be explained by the increased edge sites and the reduced free surface Ni atoms due to the growth of the carbon network.

To address the second issue, it is well-known that NiO and MgO can form a $Ni_xMg_{1-x}O$ solid solution in a wide composition range due to their similar crystal structures. However, MgO may be segregated from NiO in reducing atmospheres at high temperatures.[40−42] Moreover, our SAED patterns show that the rock salt phase exists at much higher temperatures for MgO-modified NiO. To provide further insights into this problem, we first compared the total reduction energy of MgO and NiO as defined by eq 3

$$E_{\text{reduction}} = E_{\text{M}} + 0.5 \times E_{\text{O}_2} - E_{\text{MO}} \quad (3)$$

where M stands for Mg or Ni. The computed reduction energies are 1.53 and 4.15 eV for NiO and MgO, respectively. Due to the much higher reduction energy of MgO, the reduction of MgO will not occur under our experimental conditions. To address the effects of MgO addition on the stability of the $Ni_xMg_{1-x}O$ solid solution, we further compare the neutral oxygen vacancy (NOV) formation energies of NiO, MgO, and $Ni_xMg_{1-x}O$ solid solution using a 64-atom supercell. The MgO modification is modeled by replacing one Ni atom by a Mg atom, resulting in an MgO concentration of ∼3.1%, which is close to its experimental value. The NOV formation energy is calculated by eq 4

$$E_{\text{NOV}} = E_{\text{host}} - E_{\text{defect}} - 0.5 \times E_{\text{O}_2} \quad (4)$$

The results are shown in Figure 8. The calculated NOV formation energies are 6.98 and 2.89 eV for MgO and NiO,

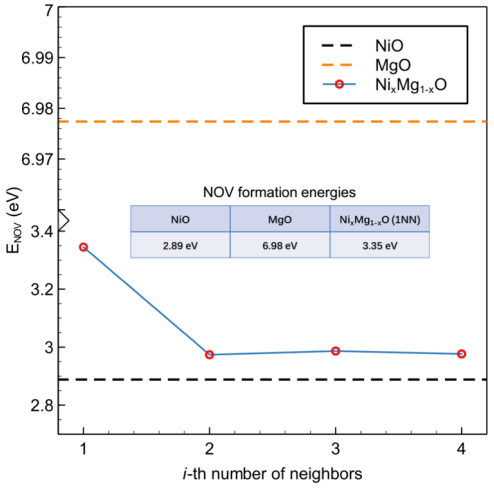

Figure 8. NOV formation energies at different oxygen sites in NiO, MgO, and $Ni_xMg_{1-x}O$ hosts.

respectively; thus, MgO modification might help stabilize the lattice oxygen sites of the NiO host. By examining the NOV formation energy change at different oxygen neighbor shells (Figure 8), we found that this is indeed the case: the incorporation of Mg atoms increases the NOV formation energy from 2.89 to 3.35 eV for the first neighbor shell,

DOI: 10.1021/acsomega.9b00958
ACS Omega 2019, 4, 8413−8420

whereas an increase of 0.1 eV is observed for all other oxygen sites. Due to the enhanced thermodynamic barrier, the MgO-modified NiO is less reducible than pristine NiO, which explains our previous experimental observation.

In short, we show that on the Ni metal surface, it is easy to form the Ni−C complex and the surface carbon shell under specified conditions. Apparently, the dynamic movement process of the solute carbon atom can be tracked by MD simulation in detail. The reason for the reduced carbon deposition by MgO incorporation is due to the enhanced oxygen site stability near the Mg defect centers.

CONCLUSIONS

In summary, in situ transmission electron microscopy reveals that the carbon deposition originates from the decomposition of the intermediate-phase Ni_3C. The modification of MgO on the NiO particle can effectively decrease the formation of graphitic layers and thus enhance the catalytic performance of NiO. This is the first experimental evidence of carbon formation originating from the decomposition of carbide by in situ TEM observation. Reactive molecular dynamics simulations clarify that the carbon deposition process involves acetylene decomposition and carbon atom reduction processes. DFT calculations show that the incorporation of MgO in the NiO host forms the $Ni_xMg_{1-x}O$ solid solution at high temperatures, which helps stabilize the lattice oxygen sites and decreases the reduced Ni metal sites and carbon decomposition.

ASSOCIATED CONTENT

Supporting Information

The Supporting Information is available free of charge on the ACS Publications website at DOI: 10.1021/acsomega.9b00958.

XRD patterns, ADF STEM image, and line-scanning profiles of elements across the particle (PDF)

NiO catalyst at 513−550 °C (AVI)

MgNiO catalyst at 500−540 °C (AVI)

Ni melting (AVI)

Solute carbon atom diffusion (AVI)

AUTHOR INFORMATION

Corresponding Authors

*E-mail: sunchunwen@binn.cas.cn (C.S.).

*E-mail: jian.chen@nrc-cnrc.gc.ca (J.C.).

*E-mail: pguan@csrc.ac.cn (P.G.).

ORCID

Chunwen Sun: 0000-0002-3610-9396

Pengfei Guan: 0000-0002-7679-6768

Notes

The authors declare no competing financial interest.

ACKNOWLEDGMENTS

The authors acknowledge the financial support of the National Natural Science Foundation of China (Nos. 51672029, 51372271, and 51172275). This work was also supported by the National Key Basic Research Program of China (Grant No. 2012CB215402). P.G. and R.S. are supported by the NSAF of China (Grant No. U1530401) and also acknowledge the computational support from the Beijing Computational Science Research Center (CSRC).

REFERENCES

(1) Snoeck, J. W.; Froment, G. F.; Fowles, M. Filamentous Carbon Formation and Gasification: Thermodynamics, Driving force, Nucleation, and Steady-State Growth. *J. Catal.* **1997**, *169*, 240−249.

(2) De Jong, K. P.; Geus, J. W. Carbon Nanofibers: Catalytic Synthesis and Applications. *Catal. Rev.* **2000**, *42*, 481−510.

(3) Bengaard, H. S.; Norskov, J. K.; Sehested, J.; Clausen, B. S.; Nielsen, L. P.; Molenbroek, A. M.; Rostrup-Nielsen, J. R. Steam Reforming and Graphite Formation on Ni Catalysts. *J. Catal.* **2002**, *209*, 365−384.

(4) Chen, D.; Christensen, K. O.; Ochoa-Femandez, E.; Yu, Z. X.; Totdal, B.; Latorre, N.; Monzon, A.; Holmen, A. Synthesis of Carbon Nanofibers: Effects of Ni Crystal Size During Methane Decomposition. *J. Catal.* **2005**, *229*, 82−96.

(5) Ermakova, M. A.; Ermakov, D. Y.; Kuvshinov, G. G.; Plyasova, L. M. New Nickel Catalysts for The Formation of Filamentous Carbon in The Reaction of Methane Decomposition. *J. Catal.* **1999**, *187*, 77−84.

(6) Park, C.; Keane, M. A. Catalyst Support Effects in The Growth of Structured Carbon from The Decomposition of Ethylene over Nickel. *J. Catal.* **2004**, *221*, 386−399.

(7) Atkinson, A.; Barnett, S.; Gorte, R. J.; Irvine, J. T. S.; Mcevoy, A. J.; Mogensen, M.; Singhal, S. C.; Vohs, J. Advanced Anodes for High-Temperature Fuel Cells. *Nat. Mater.* **2004**, *3*, 17−27.

(8) Wachsman, E. D.; Lee, K. T. Lowering the Temperature of Solid Oxide Fuel Cells. *Science* **2011**, *334*, 935−939.

(9) Huang, Y. H.; Dass, R. I.; Xing, Z. L.; Goodenough, J. B. Double Perovskites as Anode Materials for Solid-Oxide Fuel Cells. *Science* **2006**, *312*, 254−257.

(10) Sun, C.; Stimming, U. Recent Anode Advances in Solid Oxide Fuel Cells. *J. Power Sources* **2007**, *171*, 247−260.

(11) Tao, S. W.; Irvine, J. T. S. A Redox-Stable Efficient Anode for Solid-Oxide Fuel Cells. *Nat. Mater.* **2003**, *2*, 320−323.

(12) Yang, W.; Ma, Z. H.; Sun, C. W.; Chen, L. Q. Core-Shell Structured $Sr_{0.88}Y_{0.08}TiO_3$-$Ce_{0.8}Sm_{0.2}O_{1.9}$ Composite as An Anode for Solid Oxide Fuel Cells Operating with CH_4. *ECS Trans.* **2013**, *57*, 1313−1319.

(13) Yang, L.; Wang, S.; Blinn, K.; Liu, M.; Liu, Z.; Cheng, Z.; Liu, M. Enhanced Sulfur and Coking Tolerance of a Mixed Ion Conductor for SOFCs: $BaZr_{0.1}Ce_{0.7}Y_{0.2-x}Yb_xO_{3-\delta}$. *Science* **2009**, *326*, 126−129.

(14) Yang, Q.; Chai, F. T.; Ma, C.; Sun, C. W.; Shi, S. Q.; Chen, L. Q. Enhanced Coking Tolerance of A MgO-Modified Ni Cermet Anode for Hydrocarbon Fueled Solid Oxide Fuel Cells. *J. Mater. Chem. A* **2016**, *4*, 18031−18036.

(15) Zhu, H. Y.; Kee, R. J.; Janardhanan, V. M.; Deutschmann, O.; Goodwin, D. G. Modeling Elementary Heterogeneous Chemistry and Electrochemistry in Solid-Oxide Fuel Cells. *J. Electrochem. Soc.* **2005**, *152*, A2427−A2440.

(16) Helveg, S.; López-Cartes, C.; Sehested, J.; Hansen, P. L.; Clausen, B. S.; Rostrup-Nielsen, J. R.; Abild-Pedersen, F.; NØrskov, J. K. Atomic-scale imaging of carbon nanofibre growth. *Nature* **2004**, *427*, 426−429.

(17) Abild-Pedersen, F.; NØrskov, J. K.; et al. Mechanisms for catalytic carbon nanofiber growth studied by ab initio density functional theory calculations. *Phys. Rev. B* **2006**, *73*, No. 115419.

(18) Nørskov, J. K.; Bligaard, T.; Logadottir, A.; Bahn, S.; Hansen, L. B.; Bollinger, M.; Bengaard, H.; Hammer, B.; Sljivancanin, Z.; Mavrikakis, M.; Xu, Y.; Dahl, S.; Jacobsen, C. J. H. Universality in Heterogeneous Catalysis. *J. Catal.* **2002**, *209*, 275−278.

(19) Wu, J.; Shan, H.; Chen, W. L.; Gu, X.; Tao, P.; Song, C. Y.; Shang, W.; Deng, T. In Situ Environmental TEM in Imaging Gas and Liquid Phase Chemical Reactions for Materials Research. *Adv. Mater.* **2016**, *28*, 9686−9712.

(20) Wu, J.; Helveg, S.; Ullmann, S.; Peng, Z. M.; Bell, A. T. Growth of encapsulating carbon on supported Pt nanoparticles studied by in situ TEM. *J. Catal.* **2016**, *338*, 295−304.

(21) Tang, D.; Liu, C.; Yu, W. J.; Zhang, L. L.; Hou, P. X.; Li, J. C.; Li, F.; Bando, Y.; Golberg, D.; Cheng, H. M. Structural Changes in Iron Oxide and Gold Catalysts during Nucleation of Carbon

DOI: 10.1021/acsomega.9b00958
ACS Omega 2019, 4, 8413−8420

Nanotubes Studied by In Situ Transmission Electron Microscopy. *ACS Nano* **2014**, *8*, 292−301.
(22) Peng, R. R.; Xia, C. R.; Fu, Q. X.; Meng, G. Y.; Peng, D. K. Sintering and Electrical Properties of $(CeO_2)_{0.8}(Sm_2O_3)_{0.1}$ Powders Prepared by Glycine-Nitrate Process. *Mater. Lett.* **2002**, *56*, 1043−1047.
(23) Aktulga, H.; Pandit, S.; van Duin, A.; Grama, A. Reactive Molecular Dynamics: Numerical Methods and Algorithmic Techniques. *SIAM J. Sci. Comput.* **2012**, *34*, C1−C23.
(24) Mueller, J. E.; van Duin, A. C. T.; Goddard, W. A., III Application of The ReaxFF Reactive Force Field to Reactive Dynamics of Hydrocarbon Chemisorption and Decomposition. *J. Phys. Chem. C* **2010**, *114*, 5675−5685.
(25) Bal, K. M.; Neyts, E. C. On The Time Scale Associated with Monte Carlo Simulations. *J. Chem. Phys.* **2014**, *141*, No. 204104.
(26) Jeangros, Q.; Hansen, T. W.; Wagner, J. B.; Damsgaard, C. D.; Dunin-Borkowski, R. E.; Hébert, C.; Van herle, J.; Hessler-Wyser, A. Reduction of Nickel Oxide Particles by Hydrogen Studied in An Environmental TEM. *J. Mater. Sci.* **2013**, *48*, 2893−2907.
(27) Krause, M.; Melkhanova, S.; Hübner, R.; Haluska, M.; Gemming, S. Phase Transitions in C:Ni Nanocomposite Templates during Diameter-Selective CVD Synthesis of SWCNTs. *Phys. Status Solidi B* **2017**, *254*, No. 1700228.
(28) Manion, J. A. Evaluated Enthalpies of Formation of the Stable Closed Shell C1 and C2 Chlorinated Hydrocarbons. *J. Phys. Chem. Ref. Data* **2002**, *31*, 123−172.
(29) *Lax D'Ans, Taschenbuch für Chemiker und Physiker, Band III: Element, anorganische Verbindungen und Materialien, Minerale*; Springer: Berlin, Heidelberg, 1998.
(30) Demuth, J. E. The Interaction of Acetylene with Ni (111), Chemisorbed Oxygen on Ni (111), and NiO; The Formation of CH Species on Chemically Modified Ni (111) Surfaces. *Surf. Sci.* **1977**, *69*, 365−384.
(31) Hofmann, S.; Sharma, R.; Ducati, C.; Du, G.; et al. In situ Observations of Catalyst Dynamics during Surface-Bound Carbon nanotube Nucleation. *Nano Lett.* **2007**, *7*, 602−608.
(32) Pigos, E.; Penev, E. P.; Ribas, M. A.; Sharma, R.; Yakobson, B. I.; Harutyunyan, A. R. Carbon Nanotube Nucleation Driven by Catalyst Morphology Dynamics. *ACS Nano* **2011**, *5*, 10096−10101.
(33) Moseler, M.; Cervantes-Sodi, F.; Hofmann, S.; Csanyi, G.; Ferrari, A. C. Dynamic Catalyst Restructuring during Carbon Nanotube Growth. *ACS Nano* **2010**, *4*, 7587−7595.
(34) Rao, R.; Sharma, R.; Abild-Pedersen, F.; Norskov, J. K.; Harutyunyan, A. R. Insights into Carbon Nanotube Nucleation: Cap Formation Governed by Catalyst Interfacial Step Flow. *Sci. Rep.* **2015**, *4*, No. 6510.
(35) Desai, P. D. Thermodynamic Properties of Nickel. *Int. J. Thermophys.* **1987**, *8*, 763−780.
(36) Singleton, M.; Nash, P. The C-Ni (Carbon-Nickel) System. *Bull. Alloy Phase Diagrams* **1989**, *10*, 121−126.
(37) Magnin, Y.; Zappelli, A.; Amara, H.; Ducastelle, F.; Bichara, C. Size Dependent Phase Diagrams of Nickel-Carbon Nanoparticles. *Phys. Rev. Lett.* **2015**, *115*, No. 205502.
(38) Bohm, H. Modulated Structures at Phase Transitions. *Am. Mineral.* **1983**, *68*, 11−17.
(39) Heracleous, E.; Lemonidou, A. A. Ni-Me-O Mixed Metal Oxides for the Effective Oxidative Dehydrogenation of Ethane to Ethylene-Effect of Promoting Metal Me. *J. Catal.* **2010**, *270*, 67−75.
(40) Yu, M. J.; Zhu, K.; Liu, Z.; Xiao, H.; Deng, W.; Zhou, X. Carbon Dioxide Reforming of Methane over Promoted $Ni_xMg_{1-x}O$ (111) Platelet Catalyst Derived from Solvothermal Synthesis. *Appl. Catal., B* **2014**, *148*−*149*, 177−190.
(41) Hu, Y. H. Solid-Solution Catalysts for CO_2 Reforming of Methane. *Catal. Today* **2009**, *148*, 206−211.
(42) Hu, Y. H.; Ruckenstein, E. Binary MgO-Based Solid Solution Catalysts for Methane Coversion to Syngas. *Catal. Rev.* **2002**, *44*, 423−453.

DOI: 10.1021/acsomega.9b00958
ACS Omega 2019, 4, 8413−8420